RSC Advances

PAPER

View Article Online
View Journal | View Issue

Check for updates

Cite this: *RSC Adv.*, 2019, **9**, 16235

Graphene tailored by Fe_3O_4 nanoparticles: low-adhesive and durable superhydrophobic coatings†

Muqiu Wu,[a] Rong An, *[ab] Sudheer Kumar Yadav*[a] and Xiaohong Jiang[c]

Received 15th March 2019
Accepted 18th May 2019

DOI: 10.1039/c9ra02008j

rsc.li/rsc-advances

This study reports stable superhydrophobic Fe_3O_4/graphene hybrid coatings prepared by spin coating of the Fe_3O_4/graphene/PDMS mixed solution on titanium substrates. By tailoring graphene sheets with Fe_3O_4 nanoparticles, the superhydrophobicity of graphene platelets was largely enhanced with a water contact angle of 164° and sliding angle <2°. Fe_3O_4 nanoparticles interact with FLG sheets *via* Fe–O–C covalent link, to form a graphene micro-sheet pinned strongly by nano-sized Fe_3O_4. The newly-formed micro/nano-structured sheets interact with each other *via* strong dipole–dipole attractions among Fe_3O_4 nanoparticles, confirmed by the blue shifts of G band observed in Raman spectra. The strongly interactive micro/nano-structured sheets are responsible for the improvement of both the surface hydrophobicity and the durability towards water impacting. The obtained hybrid coatings possess excellent durability in various environments, such as acidic and basic aqueous solutions, simulating ocean water. And also the coatings can retain their stable superhydrophobicity in Cassie–Baxter state even after annealing at 250 °C or refrigerating at −39 °C for 10 h. We employed an AFM to probe nanoscale adhesion forces to examine further the ability of the as-prepared coatings to resist the initial formation of water layers which reflects the ability to prevent the water spreading. The most superhydrophobic and durable hybrid coating with 1.8 g Fe_3O_4, shows the smallest adhesion force, as expected, indicating this surface possesses the weakest initial water adhesive strength. The resulting low-adhesive superhydrophobic coating shows a good self-cleaning ability. This fabrication of low-adhesive and durable superhydrophobic Fe_3O_4/FLG hybrid coatings advances a better understanding of the physics of wetting and yield a prospective candidate for various practical applications, such as self-cleaning, microfluidic devices, *etc.*

1. Introduction

Superhydrophobic surfaces with a water contact angle > 150°[1,2] have been increasingly attractive because of their applications, ranging from self-cleaning, anti-fogging surfaces to efficient water/oil separation and dropwise condensation, water harvesting, *etc.*[3–9] In nature, many surfaces such as the lotus leaf are endowed with superhydrophobicity, arising from its low surface-energy wax and dual-sized surface roughness.

Graphene is a hydrophobic surface, composed of single-atom-thick carbon atoms arranged in a hexagonal lattice[10] with light weight,[10,11] while it is obvious the hydrophobicity of graphene needs to be enhanced by modifications.[12] Meanwhile, the direct use of the graphene to make a hydrophobic surface suffered limitations, because the structure of graphene sheets is fragile and easily peeled-off by water drops. The poor durability and mechanical strength of the graphene result from weak physical interactions[13] among the graphene sheets. Research efforts on exploiting superhydrophobic surfaces were focused on constructing hierarchically micro/nano structures, as well as modifying surfaces by inorganic/organic oxides or fluorides with low surface energy.[14–19]

The physical strategy is able to maintain the physicochemical properties of the graphene surface, with few side effects on the surrounding environment. The design of micro/nanostructures[20,21] is considered to be a good approach to enhance the surface hydrophobicity. For example, reed leaf-inspired graphene films with grooved hierarchical structures were created by photolithography and

---

[a] *Herbert Gleiter Institute of Nanoscience, Nanjing University of Science and Technology, Nanjing 210094, P. R. China. E-mail: ran@njust.edu.cn; Fax: +86-25-83403400; Tel: +86-25-83403400*

[b] *Center for Nanotechnology and Physical Institute, University of Münster, 48149 Münster, Germany*

[c] *International Chinese-Belarusian Scientific Laboratory on Vacuum-Plasma Technology, Nanjing University of Science and Technology, Nanjing 210094, P. R. China*

† Electronic supplementary information (ESI) available: Water static contact angles on bare FLG coatings, but with varying amount of FLG; bare Fe_3O_4 coatings, but with varying amount of FLG; the hybrid coatings with the same amount of Fe_3O_4 and varying amounts of FLG. SEM images of bare Fe_3O_4, FLG, and Fe_3O_4/FLG hybrid coatings at low resolution, XPS analysis, water adhesion, the self-cleaning performance of hybrid coatings and a video showing the resistance of Fe_3O_4-1.8 coating to water impacting. See DOI: 10.1039/c9ra02008j

laser holography technologies, showing anisotropic superhydrophobicity.[22] Spark plasma sintering was employed to synthesize 3-dimensional, superhydrophobic, reduced graphene oxide with unique hierarchical structures.[23] A laser-induced graphene method in controlled atmospheres was employed to produce 3D porous graphene structures to tune the surface wetting from superhydrophilic to superhydrophobic.[24]

Various low-surface-energy organic molecules have also been developed to modify graphene surfaces, to fabricate superhydrophobic surfaces.[25,26] However, surface properties can be altered by these modifications in many cases, and the functional groups are susceptible to oxidation, hydrolyzation, and thermal degradation.[27] Introducing fluorine-groups *via* the lower surface energy of C–F bonds is an effective modification of graphene- or carbon-based materials, to achieve superhydrophobicity.[28] For example, a superhydrophobic carbon nanotube film were created successfully *via* functionalization with poly(tetrafluoroethylene)[29] or fluoroalkylsilane[30] coatings. The hybrid aerogel consisting of graphene oxide, cellulose nanofibrils, and silica nanoparticles, showed excellent superhydrophobicity after fluorination.[31] Teflon coated graphene building blocks were used to create a superhydrophobic surface, showing good water repellency even under droplet impact conditions.[32] However, fluorides would cause mortality in mammals and birds, as well as extremely high pulmonary toxicity, *etc.*[33]

It is noteworthy that inorganic oxides are often-desired modifiers that with low surface energy and stable, and can improve the surface hydrophobicity in a controllable manner. For example, a surface roughness induced superhydrophobicity of graphene foam was reported by incorporating SiO_2 nanoparticles onto graphene sheets.[34] A stable superhydrophobic surface was achieved *via* coating with zinc oxide on aligned carbon nanotubes.[35] Magnetic iron oxide, Fe_3O_4 nanoparticles[36,37] exhibit hydrophobicity with a large surface area to volume ratio,[38,39] and chemical stability, as well as low toxicity.[40]

This gave us a hint that Fe_3O_4 nanoparticles could be employed as a binder to fix the fragile graphene sheets by the strong dipole–dipole attractions, to significantly improve the surface durability towards drop impact. And graphene is a perfect support for anchoring Fe_3O_4 nanoparticles due to the 2D-morphology,[41] which can help prevent the aggregation of Fe_3O_4 nanoparticles. The Fe_3O_4/graphene hybrids are oxidization-resistant, which is beneficial for practical applications with the presence of oxygen-relevant matter. We thus modified micro-sized few-layer graphene (FLG) platelets with Fe_3O_4 nanoparticles, enhancing interactions among graphene sheets, to achieve durable superhydrophobic Fe_3O_4/FLG hybrid coatings. In addition, our previous findings show the normal adhesion force determines the initial adhesive strength of biomolecules.[42] This inspired us that the low adhesion force of a surface would show a positive effect on the surface repellency to water. So we also investigated adhesion forces of Fe_3O_4/FLG hybrid coatings using atomic force microscopy (AFM) to examine the surface initial adhesion to water molecules.

2. Experimental section

2.1. Materials

We purchased titanium foil (thickness 0.25 mm, 99.7% trace metals basis), from Sigma Aldrich Trading Co. Ltd, USA. Few-layer graphene (FLG) platelets were from Ji Cang Nano Technology Co. Ltd., China. PDMS (poly(dimethylsiloxane), SYLGARD 184), was obtained from Dow Corning, USA, and hexane (≥97.0%), was from Sinopharm Chemical Reagent Co. Ltd., China. For the synthesis of Fe_3O_4, we purchased $Fe(NO_3)_3\cdot 9H_2O$ (99.0%) from Energy Chemical, $FeSO_4\cdot 7H_2O$ (99.0%) from Kelong Chemical, and ammonia solution (25–28%) from Lingfeng Chemical Reagent Co. Ltd, China. The Fe_3O_4 nanoparticles were synthesized by the methods as reported previously.[43]

2.2. Preparation of superhydrophobic Fe_3O_4/FLG hybrid coatings

The pristine Ti substrate, was rinsed with ethanol, under ultrasonic irradiation and dried by nitrogen. The spin coating was used to prepare Fe_3O_4/FLG hybrid coatings on bare clean Ti substrates. Different Fe_3O_4/FLG hybrid coating solutions were prepared by varying the amount of Fe_3O_4: 1 g PDMS, 0.1 g FLG, and 0.1–2.1 g Fe_3O_4 were well dispersed in 20 mL hexane under sonication. Once the entire Ti substrates were visibly covered by the as-prepared solution films, kept for 25 s, the substrate was accelerated to 500 rpm and maintained for 5 s. After the solvent hexane was mostly evaporated, the coating layers were cured at 80 °C under vacuum for 2 h to obtain Fe_3O_4/FLG hybrid coatings. The prepared coatings are denoted as 0.1 Fe_3O_4 + 0.1 FLG, 0.5 Fe_3O_4 + 0.1 FLG, 0.7 Fe_3O_4 + 0.1 FLG, 1.0 Fe_3O_4 + 0.1 FLG, 1.2 Fe_3O_4 + 0.1 FLG, 1.5 Fe_3O_4 + 0.1 FLG, 1.8 Fe_3O_4 + 0.1 FLG, 2.1 Fe_3O_4 + 0.1 FLG, in which, different amounts of Fe_3O_4 are respectively added: 0.1, 0.5, 0.7, 1.0, 1.2, 1.5, 1.8, and 2.1 g. Here PDMS acted as a glue[44] for tethering FLG layers and Fe_3O_4 nanoparticles.

In comparison, FLG (without Fe_3O_4) and Fe_3O_4 (without FLG) coatings were prepared *via* this spin-coating method. For FLG, 0.1 g FLG and 1 g PDMS mixed in 20 mL hexane under sonication to obtain the FLG solution. It is difficult for this high-concentration FLG to be spin-coated to form stable film. The unstable FLG coating is easy to be broken because of the poor durability and mechanical strength which would be discussed later in the results and discussion. For Fe_3O_4 solutions, 1.0 g Fe_3O_4 were dispersed in hexane (20 mL) with 1 g PDMS as glue under sonication.

In addition, we compared 1.0 g Fe_3O_4 with varying amounts of FLG (0.1, 0.2, 0.3, 0.4 g) in hexane (20 mL), still with 1 g PDMS as glue. We also prepared different FLG (without Fe_3O_4) and Fe_3O_4 (without FLG) coating solutions by varying the amount of FLG (0.1, 0.5, 0.7 g), and Fe_3O_4 (0.1, 0.5, 0.7, 1.0 g) in 20 mL hexane under sonication with 1 g PDMS as glue. And the static contact angle results for these coatings are shown in ESI (Fig. S1†). We also varied the size of Fe_3O_4 nanoparticles (50.3, 99.6 nm), and mixed them respectively with FLG micro-sheets (the mass ratio is 1.8 : 0.1), while their superhydrophobicity was weakened with larger sliding angles. The hybrid coating with Fe_3O_4 nanoparticles of 50.3 nm showed a contact angle of 159° with a sliding angle of 6°, while the one with bigger Fe_3O_4 showed contact angle of 157° with a larger sliding angle of 20°. We also checked the Fe_3O_4/FLG hybrid coatings with 1.8 g Fe_3O_4 on a different substrate, *i.e.*, a glass substrate, and the sample exhibited similar superhydrophobicity (static water contact angle ~155°, sliding angle < 2°) as that on Ti substrates.

2.3. Characterization

Crystalline structures of few-layer graphene and as-synthesized Fe_3O_4 and hybrid coatings were analyzed by X-ray diffraction (XRD, Cu Kα radiation, Bruker D8, USA). Micro- and nanostructures of Fe_3O_4/graphene hybrid coatings were observed by a field emission scanning electron microscope (FE-SEM, FEI Quanta 250FEG, USA). Raman spectroscopy (InVia, Renishaw, UK) was employed to investigate the interactions[45] between Fe_3O_4 and few-layer-graphene (FLG). High Resolution Transmission Electron Microscopy (HR-TEM, Titan G2 60-300, FEI, USA, operated at 300 kV) was utilized to characterize detailed structures of bare Fe_3O_4, FLG, and Fe_3O_4/FLG hybrid with 1.8 g Fe_3O_4. Attenuated Total Reflection Fourier Transform IR (ATR-FTIR, NICOLETIS10, Thermo Fisher Scientific) spectroscopy was used to examine surface chemical changes of the samples after thermal treatments. The surface morphologies of Fe_3O_4/FLG hybrid coatings were evaluated by atomic force microscopy (AFM, Dimension Icon, Bruker, USA).

X-ray photoelectron energy spectra (XPS, SPECS Surface Nano Analysis GmbH, Germany) were recorded using a SPECS XR50 imaging X-ray photoelectron spectrometer with a non-monochromatic Al Kα X-ray source (1486.6 eV). High-resolution spectra were collected for the C 1s and O 1s peaks detected with a pass energy of 10 eV. All XPS spectra were referenced to the hydrocarbon C 1s peak at 284.8 eV. The samples were degassed under a high-vacuum condition ($<10^{-8}$ Pa) to remove the adsorbed water and oxygen, before XPS measurements.

Static contact angle measurements were performed *via* a contact angle meter (JC2000D2, Shanghai Zhongchen Digital Technic Apparatus Co. Ltd, China) using a sessile drop technique. At three different locations, a 5 μL water droplet was dispensed on the substrate to measure the static contact angle. To measure sliding angles, we deposited 7 μL droplets on the surface. The sliding angles were obtained by the controlled substrate tilting after equilibration of the initial droplet shape.

2.4. Adhesion measurements

Adhesion force measurements were performed on a Dimension Icon atomic force microscopy (AFM, Bruker) in contact mode at ambient conditions. Si_3N_4 cantilever tips (DNP-10, A tip, nominal tip radius = 20 nm, tip height = 6 μm) with a nominal spring constant of 0.35 N m^{-1} were employed throughout the measurements. The adhesion force derived in terms of tip deflection *versus* the distance of separation was acquired from the force jump during retraction, which represents the pull-off force required to separate the tip after contact.

2.5. Durability tests

The anti-corrosive test of the Fe_3O_4/FLG hybrid coating with 1.8 g Fe_3O_4 was performed by adding hydrochloric acid or sodium hydroxide solution in the probe and then carrying out contact angle analysis. We also examined the durability after the sample was exposed in fresh water and simulating ocean water for 24 h. The simulating ocean water was prepared as reported.[46] The thermal resistance was evaluated by heating the coating at 250 °C for 10 h, and we also treated the sample at −39 °C for 10 h to check its durability at low temperature.

2.6. Self-cleaning performance measurements

We evaluated the self-cleaning performance of the as-prepared superhydrophobic Fe_3O_4/FLG hybrid coatings by measuring the ability of rolling water droplets taking away the sand dust which is considered as simulating pollution particles in this work.

3. Results and discussion

3.1. Surface characterization of bare Fe_3O_4, FLG, and Fe_3O_4/FLG hybrid coatings on Ti substrates

X-ray diffraction (XRD) pattern of as-synthesized Fe_3O_4 powders is presented in Fig. S2.† The corresponding peaks at 111, 220, 311, 400, 511 and 440 planes of an inverse spinel were observed in the synthetic Fe_3O_4, indicating the octahedral crystal structure. The size of the crystallite domains for Fe_3O_4 is ~13.6 nm calculated by Debye–Scherrer's formula using XRD.

We employed PDMS as a glue (bridging agent) to tether Fe_3O_4 or FLG, or Fe_3O_4/FLG hybrids to form stable coating layers on Ti substrates. The SEM images in Fig. 1a exhibited that the FLG coatings have microscale graphene wrinkles. While after modifying the FLG with Fe_3O_4 nanoparticles, we observed a less exposure of micron-sized FLG sheets in resulted hybrid coatings. The 're-arranged' nanometer-sized Fe_3O_4 particles pinned onto surfaces of FLG sheets to endow the FLG surface with nanoscale structures. The FLG sheets and intrinsic wrinkles are more visible in the hybrid coatings with Fe_3O_4 less than 1.0 g. As we increased the amounts of Fe_3O_4 nanoparticles, the FLG sheets were gradually covered. This would be confirmed later through XRD results of hybrid coatings, in which, the C(002) diffraction peak gets weaker as the amounts of Fe_3O_4 increase. It doesn't show clearly the presence of graphene in the high-resolution SEM and AFM images, probably because the local graphene sheet was covered by Fe_3O_4 nanoparticles. While the graphene sheets do exist in all hybrid coatings, as evidenced by the low-resolution SEM images shown in Fig. S3.† AFM topographies in Fig. 1b more clearly shows that Fe_3O_4 nanoparticles were strongly pinned and/or embedded by FLG microsheets. With a more addition of Fe_3O_4, each micro-sheet of FLG would be covered by Fe_3O_4 nanoparticles to form a Fe_3O_4 pinned graphene sheet. The new-formed sheets would interact with each other *via* strong dipole–dipole attractions among Fe_3O_4 nanoparticles, and the strongly interactive sheets were expected to improve the surface durability towards drop impacts. The enhanced interaction would be later confirmed by

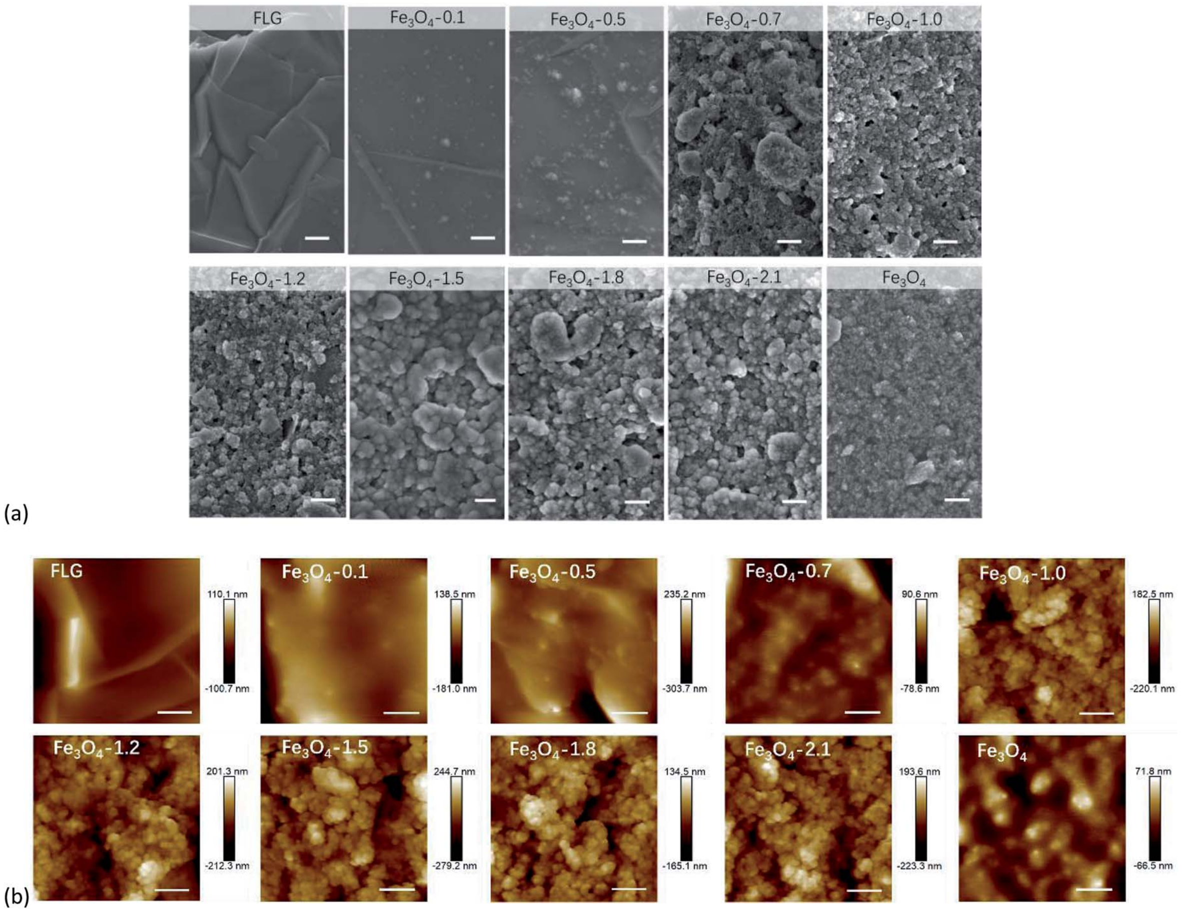

Fig. 1 (a) SEM and (b) AFM topographic images of bare Fe_3O_4, FLG, and Fe_3O_4/FLG hybrid coatings composed of 0.1 g FLG and varying amounts of Fe_3O_4 particles: 0.1, 0.5, 0.7, 1.0, 1.2, 1.5, 1.8, 2.1 g, *i.e.*, Fe_3O_4-0.1, Fe_3O_4-0.5, Fe_3O_4-0.7, Fe_3O_4-1.0, Fe_3O_4-1.2, Fe_3O_4-1.5, Fe_3O_4-1.8, Fe_3O_4-2.1. Scale bars in (a) and (b) are respectively 500 and 400 nm.

Raman spectra in Section 3.5. Graphene sheets could also act as a perfect support for anchoring Fe_3O_4 nanoparticles *via* its 2D-morphology to prevent the Fe_3O_4 nanoparticles' aggregation.

XRD patterns of FLG, and Fe_3O_4/FLG hybrid coatings displayed a C(002) diffraction peak at 26.5° (Fig. 2), while this characteristic (002) reflection of graphene gets weaker as the amount of Fe_3O_4 increased. The weakening effect suggests Fe_3O_4 nanocrystals could prevent the restacking of the graphene, resulting in less appearances of face-to-face stacking of graphene sheets.[47] At this situation, Fe_3O_4 nanoparticles act as spacers to keep FLGs separated, and hinder their aggregation caused by van der Waals forces.[47] In the same manner, the FLG sheets also reduce the aggregation of Fe_3O_4 nanoparticles. This is confirmed by the SEM observations, in which Fe_3O_4 nanoparticles are evenly distributed on the hybrid coatings.

The diffraction peaks of (311), (511), (440) lattice planes of cubic Fe_3O_4 observed in Fig. 2 were sharper with increasing Fe_3O_4. It is an indication of the raising Fe_3O_4 coverage on FLG micro-sheets, in agreement with the gradually exposed Fe_3O_4 particles in SEM observations (Fig. 1a). An appearance of the α-Ti phase[48] in 0.1–1.0 Fe_3O_4 + 0.1 FLG hybrid coatings was also observed in Fig. 2, attributed to the underlying Ti substrates, which is easily detected on thin-prepared coatings.

XPS measurements were carried out to gain further insights into surface chemical changes, and interactions of Fe_3O_4 with FLG which can be divided into the chemical link and physisorption.[47] The physical adsorption, *e.g.* the van der Waals

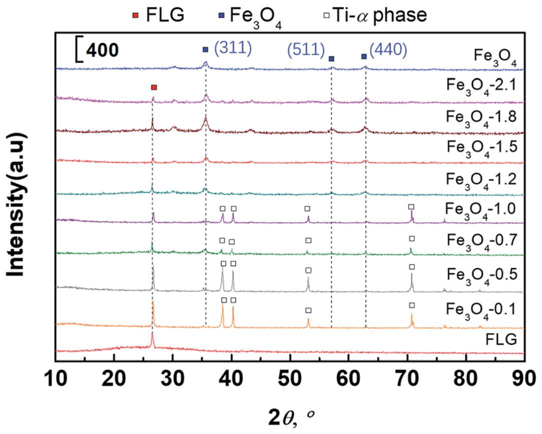

Fig. 2 XRD patterns of bare Fe_3O_4, FLG, and Fe_3O_4/FLG hybrid coatings Fe_3O_4-0.1, Fe_3O_4-0.5, Fe_3O_4-0.7, Fe_3O_4-1.0, Fe_3O_4-1.2, Fe_3O_4-1.5, Fe_3O_4-1.8, Fe_3O_4-2.1.

force, is weaker, while the chemical link can result in a much stronger interaction. As shown in Fig. 3a and Fig. S4a,† the appearance of the Si 2p (102 eV) and Si 2s (152 eV)[49,50] peaks in XPS survey spectra of all samples is dominated by the signals from the PDMS. The C, O, Fe elements were clearly revealed on the surfaces. We took high-resolution C 1s and O 1s scans to get deeper insights into the possible bond formation between Fe_3O_4 particles and graphene. In Fig. 3b, the C 1s peak centered at 284.8 eV (C–H/C–Si) in the bare Fe_3O_4 coating is attributed to the presence of PDMS. The high-resolution C 1s peaks in bare FLG and Fe_3O_4/FLG hybrid coatings (Fig. 3b and Fig. S4†) have been deconvoluted into two main contributions: the C–C/C═C & C–H/C–Si bonds at 284.8 eV assigned to aromatic rings in graphene and Si–CH_3 in PDMS,[51,52] and C–O bond at 286.2 eV due to the sp^3 free radical defects.[53]

The O 1s peak of the bare Fe_3O_4 coating can be deconvoluted to two peaks at 529.8 and 532.6 eV, which are caused respectively by O–Fe bond[47] in Fe_3O_4 and O–Si group[54] in PDMS (Fig. 3c). The deconvoluted O 1s peaks of the bare FLG coating come from O–Si (532.6 eV) in PDMS, O–H (530.8 eV),[55] and residual epoxy O–C groups (533.6 eV)[48,51,55] which agrees well with the observed C–O bond on the C 1s spectrum in Fig. 3b. Nevertheless, in the Fe_3O_4/FLG hybrid coatings, a new dominating peak appeared at 531.9 eV (middle panel in Fig. 3c, and Fig. S4†), arising from the Fe–O–C bond[47,56] which links the Fe_3O_4 with FLG. The formed Fe–O–C bond confirms the distinct interaction between Fe_3O_4 particles and FLG sheet, which would facilitate the enhanced durability in FLG sheets pinned by Fe_3O_4 nanoparticles under continuous water impacting and various environmental conditions.

3.2. Surface wetting behavior

Fig. 4 demonstrates the wetting behavior of a water droplet on the surface of bare Fe_3O_4, FLG, and Fe_3O_4/FLG hybrid coatings. The water contact angles of bare FLG and Fe_3O_4/FLG hybrid coatings with 1.0, 1.2, 1.5, 1.8 and 2.1 g Fe_3O_4, were observed to lie in the

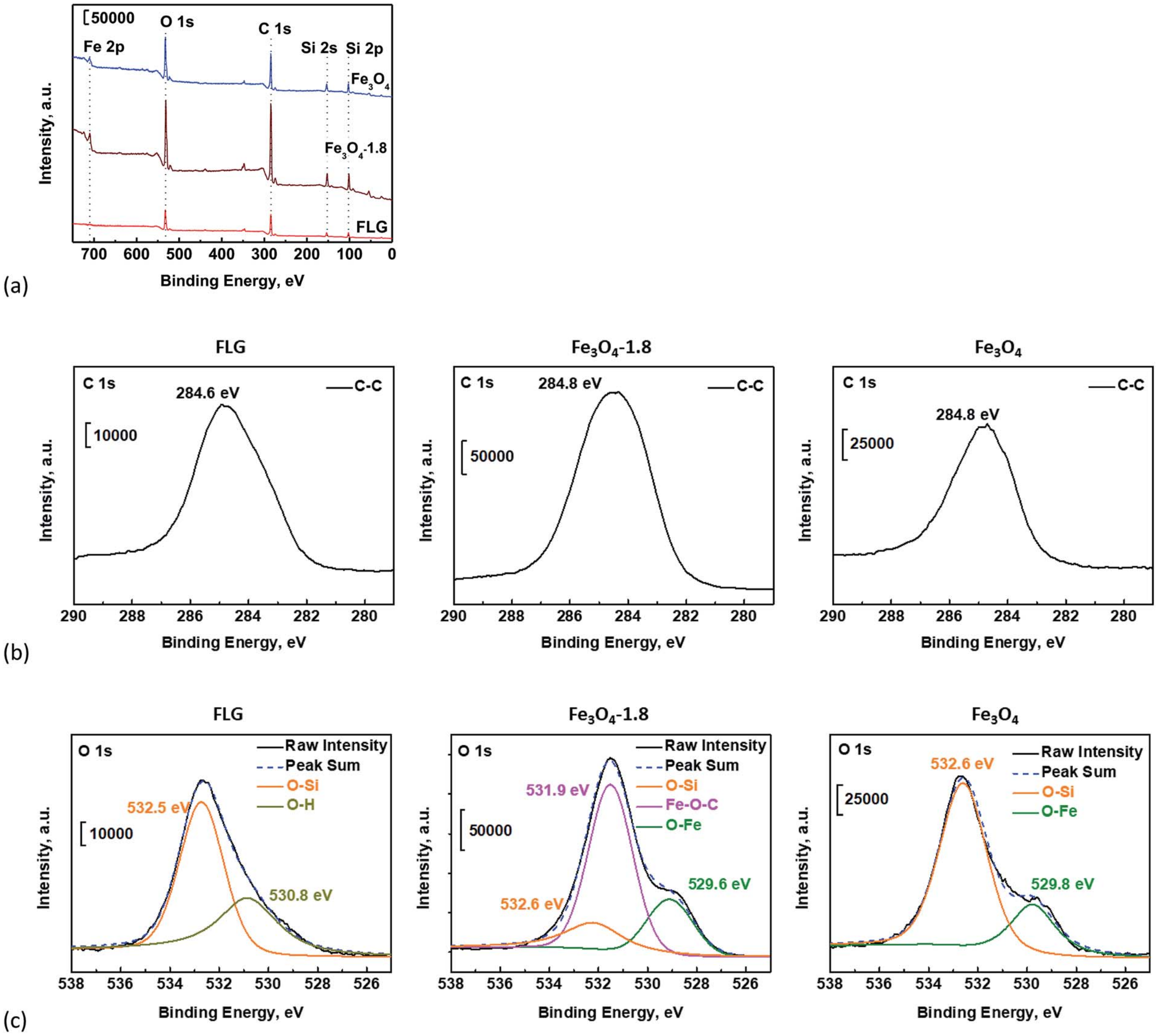

Fig. 3 (a) XPS survey spectra of bare Fe_3O_4, FLG, and Fe_3O_4/FLG hybrid coatings with 1.8 g Fe_3O_4, and their high resolution (b) C 1s, (c) O 1s spectra.

superhydrophobic range (>150°). The Fe_3O_4/FLG hybrid coatings show enhanced hydrophobic characteristics as the amount of Fe_3O_4 increases from 0.1 g to 1.8 g. The increase of Fe_3O_4 nanoparticles in the Fe_3O_4/FLG hybrid coating lead to a roughness at two length scales, which enables the amplification of the intrinsic hydrophobicity.[57] The observed increase in the contact angle from $\sim 138°$ for the hybrid coating with 0.1 g Fe_3O_4 to $\sim 164°$ for that with 1.8 g Fe_3O_4, is thus attributable to the surface roughness change caused by the varying amounts of Fe_3O_4 nanoparticles.

We used Wenzel and Cassie–Baxter models to explain the water contact angle on bare Fe_3O_4, FLG, and Fe_3O_4/FLG hybrid coatings. The apparent contact angle of the water droplet θ at the Wenzel state is calculated as:

$$\cos\theta = r\cos\theta_0 \tag{1}$$

where θ_0 is the contact angle of the water droplet on an ideal flat, homogeneous, and rigid solid surface, and r is the roughness ratio, defined by the ratio of the true surface area to the projection area. There is usually a very high adhesion between the droplet and the substrate in the case of Wenzel state.[58]

While for a Cassie drop, the contact angle θ is expressed as:

$$\cos\theta = r(1 - f_a)\cos\theta_0 - f_a \tag{2}$$

where f_a is the fraction of solid in contact with the liquid in the total projection area.

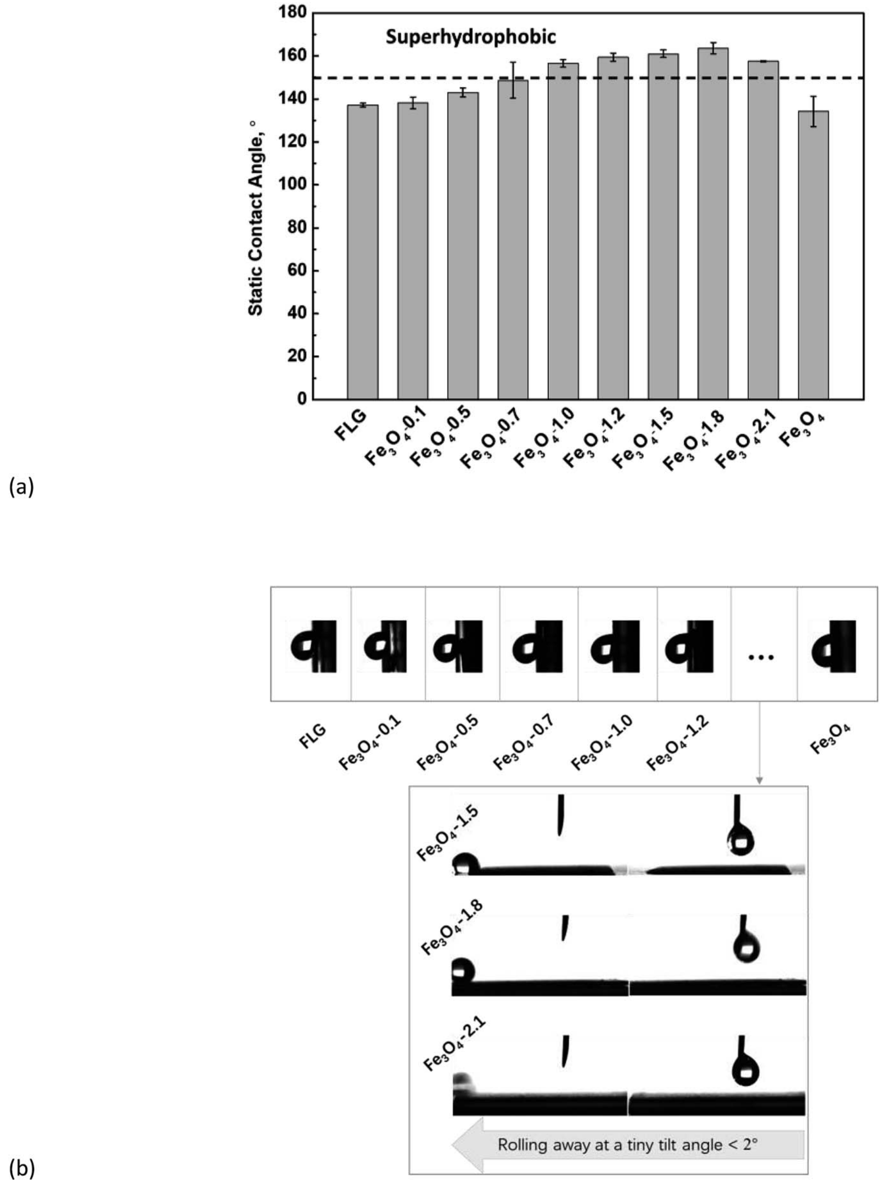

Fig. 4 (a) Variation of water static contact angles on bare Fe_3O_4, FLG, and Fe_3O_4/FLG hybrid coatings Fe_3O_4-0.1, Fe_3O_4-0.5, Fe_3O_4-0.7, Fe_3O_4-1.0, Fe_3O_4-1.2, Fe_3O_4-1.5, Fe_3O_4-1.8, Fe_3O_4-2.1. (b) Sliding angle measurements: the adhesive performance is demonstrated by a water drop clinging to the vertical coatings wall, on bare FLG, Fe_3O_4 coatings, and Fe_3O_4/FLG hybrid coatings with 0.1, 0.5, 0.7, 1.0, 1.2 g Fe_3O_4. Droplet quickly rolled off from Fe_3O_4/FLG hybrid coatings with 1.5, 1.8, and 2.1 g Fe_3O_4 at a tiny sliding angle < 2°.

We performed further sliding angle measurements to decide exactly whether a water droplet contact with the coatings in the Wenzel state or Cassie–Baxter state. As shown in Fig. 4b, the bare Fe_3O_4 and FLG substrate as well as the hybrid coatings with Fe_3O_4 of 0.1–1.2 g sustain the clinging droplets as the substrate with a deposited drop is tilted, and the drop remains attached even when the substrate becomes vertical, indicating a Wenzel state. Since the roughness ratio r in eqn (1) is always larger than 1, the inherent wettability could be amplified by the roughness effect,[59] *i.e.*, θ will be higher than θ_0 if the surface is originally hydrophobic ($\theta_0 > 90°$). An individual graphene sheet or Fe_3O_4 surface is hydrophobic, so a rougher hybrid coating is expected to display more (super)hydrophobic response. From AFM results in Fig. 5, both the surface roughness and the roughness ratio r increase in the order: Fe_3O_4-1.2 > Fe_3O_4-1.0 > Fe_3O_4-0.7 > Fe_3O_4-0.5 > Fe_3O_4-0.1 > FLG > Fe_3O_4, and their static contact angles follow this order, confirming the Wenzel model prediction. While for Fe_3O_4/FLG hybrid coatings with 1.5, 1.8, and 2.1 g Fe_3O_4, the water droplet could quickly roll off at a rather tiny sliding angle less than 2°, revealing a Cassie–Baxter state.

3.3. Surface adhesion forces and self-cleaning

As observed from the sliding angle measurements in Fig. 4b, the water droplet was strongly stick onto the substrate in Wenzel state, while in the case of a Cassie–Baxter state, the adhesion of water to the solid substrate is weak. We therefore employed AFM to probe nanoscale adhesion forces to examine further the ability of the as-prepared coatings to resist the formation of water layers. A poor resistance to the water layer formation would facilitate the water spreading. The AFM-measured adhesion force in air arises from the presence of a liquid film, such as an adsorbed water layer, that causes meniscus bridges, and available contact area, *etc.*[60] As presented in Fig. 6, the adhesion forces are smaller on Fe_3O_4-1.5, Fe_3O_4-1.8, Fe_3O_4-2.1 surfaces, respectively of 11.7 ± 0.4, 5.7 ± 0.1 and 7.9 ± 0.3 nN, implying weaker attractive forces to water, which avoids the formation of meniscus bridges, facilitating the water repellency. This is in a good agreement with our experimental observations of low adhesive water droplets on the Fe_3O_4/FLG hybrid coating surfaces (Fig. S5†): the water droplet can be pulled easily from the surfaces and not stuck to the surfaces during an approach/separation cycle, demonstrating an ultralow water-adhesive force.[61] We note that the Fe_3O_4-1.8 coating surface, shows the smallest adhesion force as expected (marked in the green circle in Fig. 6). This indicates Fe_3O_4-1.8 possesses the weakest initial water adhesive strength so that it enables the strong resistance to the formation of water layers and prevent the water spreading. While the other coatings show higher adhesion forces, indicative of poor abilities to resist the water spreading. The different adhesion forces would result in a significant difference in the water bouncing, as shown later in Fig. 7a.

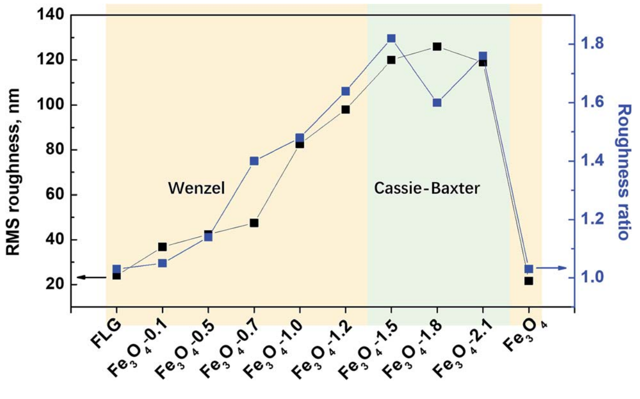

Fig. 5 AFM measured surface roughnesses of bare Fe_3O_4, FLG, and Fe_3O_4/FLG hybrid coatings Fe_3O_4-0.1, Fe_3O_4-0.5, Fe_3O_4-0.7, Fe_3O_4-1.0, Fe_3O_4-1.2, Fe_3O_4-1.5, Fe_3O_4-1.8, Fe_3O_4-2.1. RMS is the root-mean-square roughness, and the roughness ratio r was obtained from AFM topographic images (the ratio of the true surface area to the projection area).

Our previous findings shows that a low-adhesive surface would exhibit a positive effect on the self-cleaning ability, because the low adhesion enables the initial prevention[42] of the contaminants attachment. This inspired us to further evaluate the self-cleaning abilities of Fe_3O_4/FLG hybrid coatings with varying adhesive properties, and the common sand dust was chosen as a model contaminant.[62] Fe_3O_4-1.8 has shown promising self-cleaning ability, and the sand dust deposited on the surfaces was easily be taken away by sliding water droplets as indicated in Fig. S6.† Nearly no contaminant particles are left on the rolling path of the water droplet. Whereas, in the case of bare FLG, the sand dust was sticking to the surface and cannot be completely cleared off by rolling water. The water droplet is even pinned onto the bare Fe_3O_4 coating and most of the dust remained on the surface. A similar tendency, but less sand dust, was also observed to adhere to the Fe_3O_4/FLG hybrid coating surfaces with Fe_3O_4 of 0.1–1.5 g and 2.1 g.

3.4. Durability test

Inspired by a previous report that water should rapidly shed from the anti-wetting surfaces,[44] we checked the water-shielding ability of bare Fe_3O_4, FLG and Fe_3O_4/FLG hybrid coatings to evaluate the surface mechanical strength. In Fig. 7a, the bare FLG coating was observed to be broken by the water impacting,

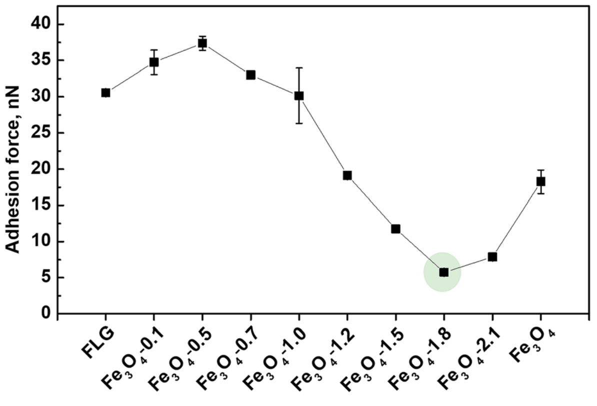

Fig. 6 AFM-measured adhesion force of bare Fe_3O_4, FLG, and Fe_3O_4/FLG hybrid coatings.

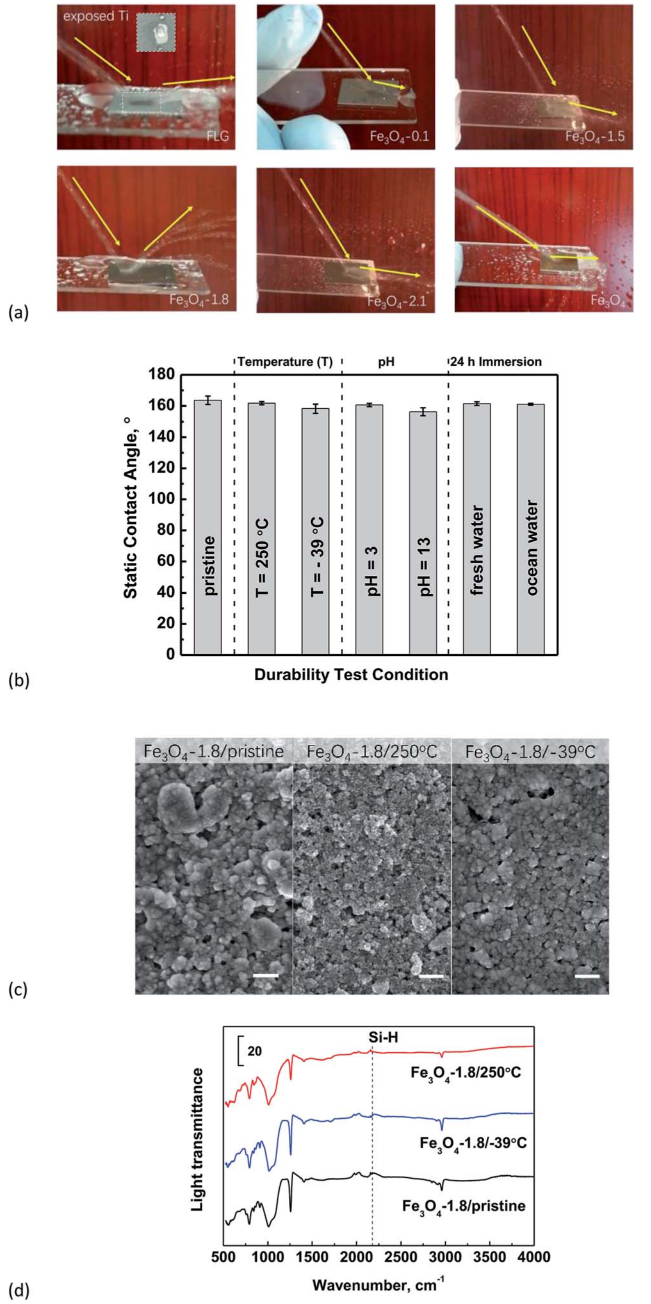

Fig. 7 (a) Continuous water impacting applied on FLG, Fe_3O_4, and Fe_3O_4/FLG hybrid coatings to show different water-shielding abilities. (b) Variation of static contact angle for Fe_3O_4-1.8 samples in different environmental conditions: after annealing and cooling the samples for 10 h; pH influences by employing acidic and basic aqueous solutions as probe water; after 24 h immersion in normal fresh water and simulating ocean water. (c) SEM images, (d) ATR-FTIR spectra of Fe_3O_4-1.8 before and after thermal treatment. Scale bars in (c) are 500 nm.

and show the exposed Ti substrate, because of its poor durability, which make the surface fragile and easily peeled-off by water droplets.[13] The bare Fe_3O_4 as expected, tends to capture the water droplets and drain them along the substrates. It is surprising that the water impacting was completely rebounded by the superhydrophobic Fe_3O_4/FLG hybrid coating with 1.8 g Fe_3O_4, showing a superior water-shielding ability, and this water bouncing is more clearly observed in the video in the ESI.† However, the superhydrophobic hybrid coating with 1.5 or 2.1 g Fe_3O_4 exhibits inelastic collisions of water impacting. The water impacting also suffered from an inelastic collision on the hybrid coatings as we decreased the amount of Fe_3O_4 to 0.1 g, and the water was observed to flow at the rim of the substrate.

As we know, super-hydrophobic surfaces are easy to lose the super-hydrophobicity under high temperature and humidity, because surface chemical groups '-X' would be oxidized/hydroxylated to –OH groups, leading to the adsorption of water.[63] And changes in the surface morphology under high temperature might weaken the surface hydrophobicity. We thus examined the thermal resistance of superhydrophobic Fe_3O_4/FLG hybrid coating with 1.8 g Fe_3O_4 (*i.e.*, Fe_3O_4-1.8) which shows the best water-shielding ability. In comparison with the non-treated Fe_3O_4-1.8 sample, the static water contact angle almost remains constant after the samples were annealed at 250 °C for 10 h (Fig. 7b), demonstrating the excellent thermal stability. They can also keep their superhydrophobic character after being frozen at −39 °C for 10 h. Through SEM images and ATR-FTIR spectra in Fig. 7c and d, no obvious structural and chemical changes were observed in Fe_3O_4-1.8 after it is refrigerated at −39 °C for 10 h, as compared to the pristine one. Consequently, the surface structural and chemical stability is responsible for maintaining the super-hydrophobic performance at −39 °C. As for the Fe_3O_4-1.8 heated at 250 °C, particles on the surface seem to be more separated in comparison with the pristine Fe_3O_4-1.8. This change in the surface morphology is due to the decomposition of the 'glue', PDMS which started to thermally decompose at around 150 °C,[64] and this was confirmed by the disappearance of Si–H bond (~2184 cm^{-1})[65] in ATR-FTIR spectra. The 250°C-heated Fe_3O_4-1.8 still kept a good superhydrophobicity, indicating that the 'glue', PDMS has almost no influence on, the wetting behavior which depends critically on the graphene micro-sheet pinned strongly by nano-sized Fe_3O_4.

In addition, the as-prepared Fe_3O_4/FLG hybrid coating, Fe_3O_4-1.8, displays excellent durability in corrosive conditions. For example, it shows good repellency with static contact angle of ~160° to acidic and basic aqueous solutions. We also explored the superhydrophobic stability of Fe_3O_4-1.8 exposed to normal fresh water and simulating ocean water for 24 h. The measured contact angle is still *ca.* 161° for the Fe_3O_4-1.8 sample which was exposed in either fresh water or simulating ocean water. And the sliding angles are less than 2° for all cases (Fig. 7b), showing a stable Cassie–Baxter state.

3.5. Enhanced interactions among FLG sheets pinned by Fe_3O_4 nanoparticles

The different interaction behavior among FLG sheets which are pinned by Fe_3O_4 nanoparticles can be confirmed by Raman measurements. It can be clearly seen that the Raman spectra (Fig. 8a) of all Fe_3O_4/FLG hybrid coatings exhibit two characteristic bands, *i.e.*, G and 2D bands, corresponding respectively to the vibration of sp^2 carbon atoms, as well as the stacking orders.[66,67] The location of G peak was used previously to study the interaction between nanoparticles and carbon nanotubes.[68] In Fig. 8b, the G band locates at 1577 cm^{-1} for bare FLG coatings, however, the addition of Fe_3O_4 induced blue shift of G band, which even shifts to 1583 cm^{-1} for Fe_3O_4-1.8 hybrid coatings. The blue shifts of the G band in Fe_3O_4/FLG hybrid coatings indicate the presence of strains due to the strong interaction[45,69] among FLG sheets pinned by Fe_3O_4 nanoparticles. The enhanced interactions among graphene sheets originate from the strong dipole–dipole attractions between pinned Fe_3O_4 nanoparticles, as shown in the schematics in Fig. 8b. The strongly interactive micro/nano-structured sheets are responsible for the improvement of both the surface hydrophobicity and the durability towards the water impacting.

It is obvious that Fe_3O_4-1.8 hybrid coatings with a pronounced blue shift, possess stronger interactions, which

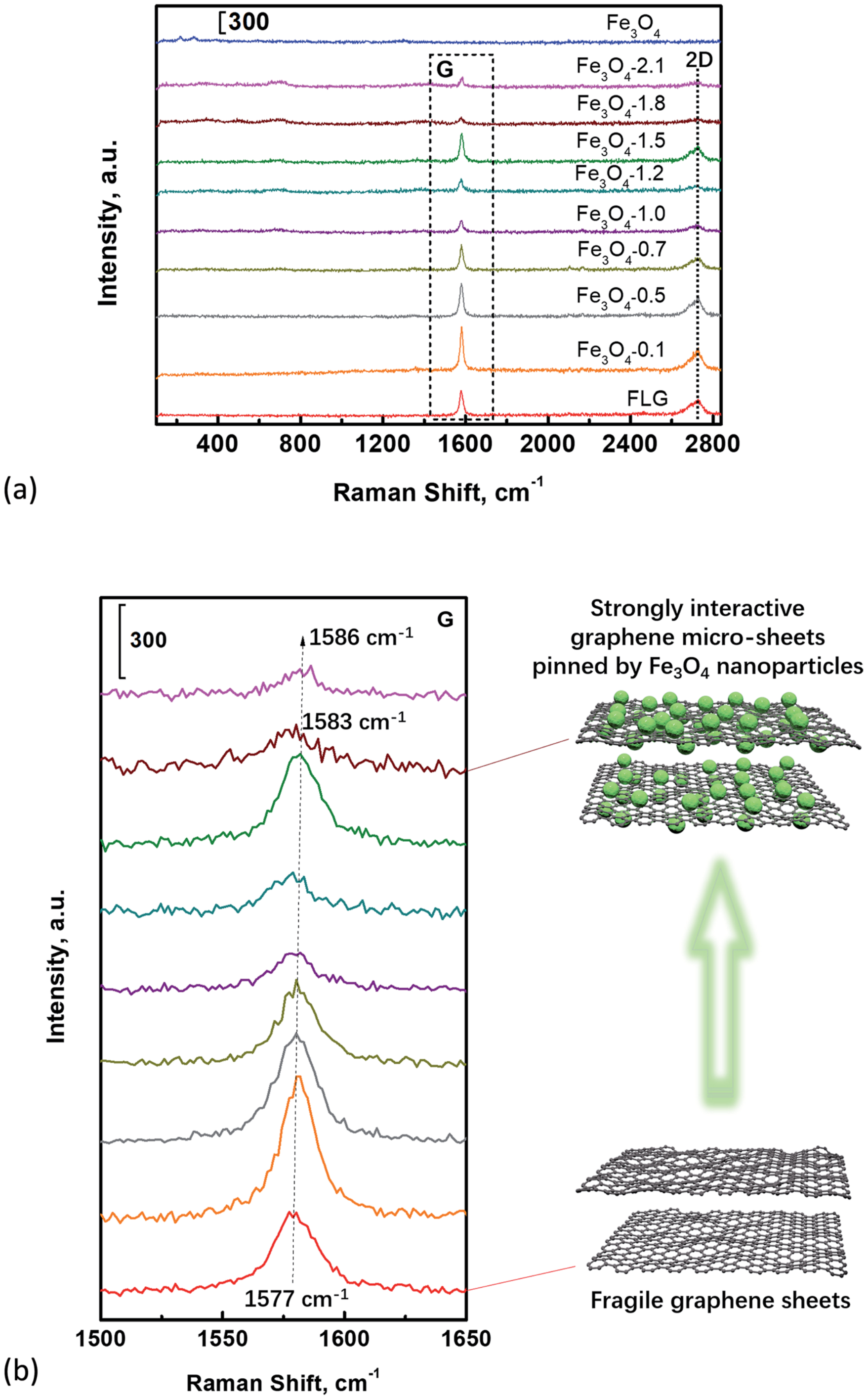

Fig. 8 (a) Raman spectra of Fe_3O_4, FLG, and Fe_3O_4/FLG hybrid coatings, (b) the enlarged G peak of graphene enclosed by the black dash square in panel (a).

ensure the excellent surface durability. We note a further increase of Fe_3O_4 into FLG sheets, *i.e.*, Fe_3O_4-2.1 also shows an enhanced blue shift, while its water-shielding ability is not as good as Fe_3O_4-1.8. It is probably due to the FLG sheets fully covered by Fe_3O_4 nanoparticles in the case of Fe_3O_4-2.1, to form merely a single level of nanostructuring surface, which is responsible for its poor water-shielding ability.

4. Conclusions

Mechanically stable superhydrophobic Fe_3O_4/graphene hybrid coatings have been successfully prepared by spin coating of the Fe_3O_4/graphene/PDMS mixed solution. Fe_3O_4 nanoparticles interact with FLG sheets *via* Fe–O–C bonds, to form a graphene micro-sheet pinned strongly by nano-sized Fe_3O_4. The formed micro/nano-structured sheets would interact with each other *via* strong dipole–dipole attractions among Fe_3O_4 nanoparticles. The resulted strongly interactive micro/nano-structured sheets facilitate to improve both the surface hydrophobicity and the durability. The mostly hydrophobic hybrid coating Fe_3O_4-1.8 can maintain the superhydrophobic property in the Cassie–Baxter state even being exposed to corrosive liquids (pH = 3 or 13). Meanwhile, the coatings are thermally stable up to 250 °C, and can still retain superhydrophobic at −39 °C. AFM-probed nanoscale adhesion force in Fe_3O_4-1.8 surface is the smallest, indicating the weakest initial water adhesive strength. The water droplets can roll around freely on this low-adhesive superhydrophobic surface, and remove dust easily, providing excellent self-cleaning performance. The superhydrophobic Fe_3O_4/graphene hybrid coatings enrich the understanding of wettability for complex surfaces and widen potential applications in various industries and daily life.

Author contributions

Authors M. Q. Wu and R. An contributed equally to this work. All authors have given approval to the final version of the manuscript.

Conflicts of interest

There are no conflicts to declare.

Acknowledgements

We are grateful to the support from the National Natural Science Foundation of China (Grant No. 21606131, 21676137), the Fundamental Research Funds for the Central Universities (Grant No. 30918015104) and open-end fund for the large instruments of Nanjing University of Science and Technology. We thank Professor Tianchi Wang for the access to his contact angle meter, and Professor Tao Feng for the access to his XPS instrument.

References

1 L. Feng, S. H. Li, H. J. Li, J. Zhai, Y. L. Song, L. Jiang and D. B. Zhu, *Angew. Chem., Int. Ed.*, 2002, **41**, 1221–1223.

2 D. D. Nguyen, N.-H. Tai, S.-B. Lee and W.-S. Kuo, *Energy Environ. Sci.*, 2012, **5**, 7908–7912.

3 X.-M. Li, D. Reinhoudt and M. Crego-Calama, *Chem. Soc. Rev.*, 2007, **36**, 1350–1368.

4 Z. Sun, T. Liao, K. Liu, L. Jiang, J. H. Kim and S. X. Dou, *Small*, 2014, **10**, 3001–3006.

5 R. Wen, S. Xu, D. Zhao, Y.-C. Lee, X. Ma and R. Yang, *ACS Appl. Mater. Interfaces*, 2017, **9**, 44911–44921.

6 X. Chen, J. Wu, R. Ma, M. Hua, N. Koratkar, S. Yao and Z. Wang, *Adv. Funct. Mater.*, 2011, **21**, 4617–4623.

7 N. Miljkovic, R. Enright, Y. Nam, K. Lopez, N. Dou, J. Sack and E. N. Wang, *Nano Lett.*, 2013, **13**, 179–187.

8 N. Miljkovic, R. Enright and E. N. Wang, *ACS Nano*, 2012, **6**, 1776–1785.

9 Y. Fu, B. Jin, Q. Zhang, X. Zhan and F. Chen, *ACS Appl. Mater. Interfaces*, 2017, **9**, 30161–30170.

10 X. Dong, J. Chen, Y. Ma, J. Wang, M. B. Chan-Park, X. Liu, L. Wang, W. Huang and P. Chen, *Chem. Commun.*, 2012, **48**, 10660–10662.

11 X. Zheng, J. Feng, Y. Zong, H. Miao, X. Hu, J. Bai and X. Li, *J. Mater. Chem. C*, 2015, **3**, 4452–4463.

12 D. Jing, Z. Yao, T. Yang, L. Jiang and C. Shen, *Sci. Rep.*, 2013, **3**, 1733.

13 K. Seo, M. Kim and D. H. Kim, *Carbon*, 2014, **68**, 583–596.

14 P. Wang, T. Zhao, R. Bian, G. Wang and H. Liu, *ACS Nano*, 2017, **11**, 12385–12391.

15 Y. Wang and X. Gong, *Adv. Mater. Interfaces*, 2017, **4**, 1700190.

16 Y. Tang, Q. Zhang, X. Zhan and F. Chen, *Soft Matter*, 2015, **11**, 4540–4550.

17 Y. Fu, J. Jiang, Q. Zhang, X. Zhan and F. Chen, *J. Mater. Chem. A*, 2017, **5**, 275–284.

18 Q. Rao, A. Li, J. Zhang, J. Jiang, Q. Zhang, X. Zhan and F. Chen, *J. Mater. Chem. A*, 2019, **7**, 2172–2183.

19 M. I. Jamil, A. Ali, F. Haq, Q. Zhang, X. Zhan and F. Chen, *Langmuir*, 2018, **34**, 15425–15444.

20 L. Feng, S. H. Li, Y. S. Li, H. J. Li, L. J. Zhang, J. Zhai, Y. L. Song, B. Q. Liu, L. Jiang and D. B. Zhu, *Adv. Mater.*, 2002, **14**, 1857–1860.

21 W. Ming, D. Wu, R. van Benthem and G. de With, *Nano Lett.*, 2005, **5**, 2298–2301.

22 H.-B. Jiang, Y.-Q. Liu, Y.-L. Zhang, Y. Liu, X.-Y. Fu, D.-D. Han, Y.-Y. Song, L. Ren and H.-B. Sun, *ACS Appl. Mater. Interfaces*, 2018, **10**, 18416–18425.

23 J. Wu, Z. Li, X. Xie, K. Tao, C. Liu, K. A. Khor, J. Miao and L. K. Norford, *J. Mater. Chem. A*, 2018, **6**, 478–488.

24 Y. Li, D. X. Luong, J. Zhang, Y. R. Tarkunde, C. Kittrell, F. Sargunaraj, Y. Ji, C. J. Arnusch and J. M. Tour, *Adv. Mater.*, 2017, **29**, 1700496.

25 Y. Lin, G. J. Ehlert, C. Bukowsky and H. A. Sodano, *ACS Appl. Mater. Interfaces*, 2011, **3**, 2200–2203.

26 Z.-H. Mo, Z. Luo, Q. Huang, J.-P. Deng and Y.-X. Wu, *Appl. Surf. Sci.*, 2018, **440**, 359–368.

27 S. Chen and S. Jiang, *Adv. Mater.*, 2008, **20**, 335–338.

28 K. Jayaramulu, K. K. R. Datta, C. Roesler, M. Petr, M. Otyepka, R. Zboril and R. A. Fischer, *Angew. Chem., Int. Ed.*, 2016, **55**, 1178–1182.

29 K. K. S. Lau, J. Bico, K. B. K. Teo, M. Chhowalla, G. A. J. Amaratunga, W. I. Milne, G. H. McKinley and K. K. Gleason, *Nano Lett.*, 2003, **3**, 1701–1705.

30 H. J. Li, X. B. Wang, Y. L. Song, Y. Q. Liu, Q. S. Li, L. Jiang and D. B. Zhu, *Angew. Chem., Int. Ed.*, 2001, **40**, 1743–1746.

31 H.-Y. Mi, X. Jing, H.-X. Huang, X.-F. Peng and L.-S. Turng, *Ind. Eng. Chem. Res.*, 2018, **57**, 1745–1755.

32 E. Singh, Z. Chen, F. Houshmand, W. Ren, Y. Peles, H.-M. Cheng and N. Koratkar, *Small*, 2013, **9**, 75–80.

33 X. Li, J. Wang, Y. Zhao and X. Zhang, *ACS Appl. Mater. Interfaces*, 2018, **10**, 16901–16910.

34 S. Yang, L. Chen, C. Wang, M. Rana and P.-C. Ma, *J. Colloid Interface Sci.*, 2017, **508**, 254–262.

35 L. Huang, S. P. Lau, H. Y. Yang, E. S. P. Leong, S. F. Yu and S. Prawer, *J. Phys. Chem. B*, 2005, **109**, 7746–7748.

36 H. Alamri, A. Al-Shahrani, E. Bovero, T. Khaldi, G. Alabedi, W. Obaid, I. Al-Taie and A. Fihri, *J. Colloid Interface Sci.*, 2018, **513**, 349–356.

37 T. Cheng, R. He, Q. Zhang, X. Zhan and F. Chen, *J. Mater. Chem. A*, 2015, **3**, 21637–21646.

38 Y. I. Park, Y. Piao, N. Lee, B. Yoo, B. H. Kim, S. H. Choi and T. Hyeon, *J. Mater. Chem.*, 2011, **21**, 11472–11477.

39 A. K. Gupta and M. Gupta, *Biomaterials*, 2005, **26**, 3995–4021.

40 J. Li, C.-Y. Hong, S.-X. Wu, H. Liang, L.-P. Wang, G. Huang, X. Chen, H.-H. Yang, D. Shangguan and W. Tan, *J. Am. Chem. Soc.*, 2015, **137**, 11210–11213.

41 W. Baaziz, T.-P. Lai, D.-V. Cuong, G. Melinte, I. Janowska, V. Papaefthimiou, O. Ersen, S. Zafeiratos, D. Begin, S. Begin-Colin and C. Pham-Huu, *J. Mater. Chem. A*, 2014, **2**, 2690–2700.

42 R. An, Y. Dong, J. Zhu and C. Rao, *Colloids Surf., B*, 2017, **159**, 108–117.

43 S. Sahu and R. K. Dutta, *J. Magn. Magn. Mater.*, 2011, **323**, 980–987.

44 M. Cao, D. Guo, C. Yu, K. Li, M. Liu and L. Jiang, *ACS Appl. Mater. Interfaces*, 2016, **8**, 3615–3623.

45 Y. Chen, S. Han, X. Li, Z. Zhang and S. Ma, *Inorg. Chem.*, 2014, **53**, 10006–10008.

46 *Standard practice for the preparation of substitute oceanwater, ASTM Standard D 1141*, ASTM International, 2013.

47 J. Zhou, H. Song, L. Ma and X. Chen, *RSC Adv.*, 2011, **1**, 782–791.

48 R. An, G. Zhou, Y. Zhu, W. Zhu, L. Huang and F. U. Shah, *Adv. Mater. Interfaces*, 2018, **5**, 1800263.

49 Y. Xue, Y. Liu, F. Lu, J. Qu, H. Chen and L. Dai, *J. Phys. Chem. Lett.*, 2012, **3**, 1607–1612.

50 A. Papra, A. Bernard, D. Juncker, N. B. Larsen, B. Michel and E. Delamarche, *Langmuir*, 2001, **17**, 4090–4095.

51 Z. Rashid, I. Atay, S. Soydan, M. B. Yagci, A. Jonas, E. Yilgor, A. Kiraz and I. Yilgor, *Appl. Surf. Sci.*, 2018, **441**, 841–852.

52 C. Mattevi, G. Eda, S. Agnoli, S. Miller, K. A. Mkhoyan, O. Celik, D. Mastrogiovanni, G. Granozzi, E. Garfunkel and M. Chhowalla, *Adv. Funct. Mater.*, 2009, **19**, 2577–2583.

53 D. Q. Yang and E. Sacher, *Langmuir*, 2006, **22**, 860–862.

54 J. Yu, H. Yu, B. Cheng, Z. Xiujian, Y. Jiaguo and H. Wingkei, *J. Phys. Chem. B*, 2003, **107**, 13871–13879.

55 J. Hu, H. Diao, W. Luo and Y.-F. Song, *Chem.–Eur. J.*, 2017, **23**, 8729–8735.

56 Y. Liu, X. Liu, Y. Zhao and D. D. Dionysiou, *Appl. Catal., B*, 2017, **213**, 74–86.

57 L. Feng, Y. Zhang, J. Xi, Y. Zhu, N. Wang, F. Xia and L. Jiang, *Langmuir*, 2008, **24**, 4114–4119.

58 J. Yong, F. Chen, Q. Yang, Z. Jiang and X. Hou, *Adv. Mater. Interfaces*, 2018, **5**, 1701370.

59 J. Rafiee, M. A. Rafiee, Z.-Z. Yu and N. Koratkar, *Adv. Mater.*, 2010, **22**, 2151–2154.

60 B. Bhushan and E. K. Her, *Langmuir*, 2010, **26**, 8207–8217.

61 C. Wei, F. Dai, L. Lin, Z. An, Y. He, X. Chen, L. Chen and Y. Zhao, *J. Membr. Sci.*, 2018, **555**, 220–228.

62 H. Liu, P. Zhang, M. Liu, S. Wang and L. Jiang, *Adv. Mater.*, 2013, **25**, 4477–4481.

63 Y. Zhang, B. Dong, S. Wang, L. Zhao, L. Wan and E. Wang, *RSC Adv.*, 2017, **7**, 47357–47365.

64 G. Camino, S. M. Lomakin and M. Lazzari, *Polymer*, 2001, **42**, 2395–2402.

65 A. C. M. Kuo, Poly(dimethylsiloxane), in *Polymer data handbook*, ed. J. E.Mark, Oxford University Press, New York, 1999, p. 412.

66 Y. y. Wang, Z. h. Ni, T. Yu, Z. X. Shen, H. m. Wang, Y. h. Wu, W. Chen and A. T. Shen Wee, *J. Phys. Chem. C*, 2008, **112**, 10637–10640.

67 M. A. Pimenta, G. Dresselhaus, M. S. Dresselhaus, L. G. Cancado, A. Jorio and R. Saito, *Phys. Chem. Chem. Phys.*, 2007, **9**, 1276–1290.

68 R. Kitaura, N. Imazu, K. Kobayashi and H. Shinohara, *Nano Lett.*, 2008, **8**, 693–699.

69 V. Khare, M.-Q. Pham, N. Kumari, H.-S. Yoon, C.-S. Kim, J.-I. L. Park and S.-H. Ahn, *ACS Appl. Mater. Interfaces*, 2013, **5**, 4063–4075.